



Linking rates of slab sinking to long-term lower mantle flow and mixing

Erik van der Wiel^{*}, Douwe J.J. van Hinsbergen, Cedric Thieulot, Wim Spakman

Department of Earth Sciences, Faculty of Geosciences, Utrecht University, Utrecht, the Netherlands

ARTICLE INFO

Edited by: Dr H Thybo

Keywords:

Mantle convection
Slab sinking rates
Mantle mixing
Modelling constraints

ABSTRACT

Numerical models of Earth's mantle dynamics that aim to comply with a variety of surface observations and/or modern mantle structure, still predict a widely varying vigour of mantle flow which governs the long-term evolution of mantle structure and mixing. A yet unexplored source of intrinsic information on mantle flow characteristics are the geologically reconstructed average slab sinking rates. Here we evaluate from numerical experiments how average slab sinking rates relate to the vigour of mantle convection and mixing. We use a simplified mantle convection model and show that long-term mantle flow velocity and mixing is strongly sensitive to slab sinking rates. Models tuned to match lower mantle average sinking rates of 10–15 mm/a, yield lower mantle convection rates of only several mm/a. Furthermore, they reveal large unmixed regions in the mid-mantle which preserve 25% of 'primordial' lower mantle material after 1000 Ma, which may explain geochemical observations from hotspot volcanoes.

1. Introduction

Earth's mantle is a solid-state convecting system which governs multiple dynamic processes from deep geochemical mixing to the plate tectonics and deformation of the cold boundary layer (e.g. [Bercovici et al. 2015](#)). How mantle processes dynamically operate can only be assessed by numerical modelling of the chemical-physical system as observations of mantle dynamics are generally of an implicit kinematic nature. Numerical experiments can be of a generic nature, or can focus on the simulation of mantle convection models that comply with observations, e.g., reconstructed and active plate motions ([Coltice et al., 2013](#); [Rolf et al., 2018](#)), geochemical composition and evolution of the Earth's interior revealed by volcanic rocks ([Yan et al., 2020](#)), and/or seismological observations of modern mantle structure ([Ballmer et al., 2016](#); [Ritsema and Lekić, 2020](#)). This large variety of observational constraints has, however, not led to imposing a strong constraint on the style of mantle convection in terms of the typical flow velocity and spatial variation, or of fast/slow geochemical mixing.

An unexplored source of information on the vigour of mantle convection are the geologically reconstructed average slab sinking rates of [van der Meer et al. \(2018\)](#). These slab sinking rates were determined for the tomographically imaged tops and bottoms of slabs by dividing the imaged depth by the geological time since subduction initiation and cessation. Importantly, these rates combine geological dating of past subduction with modern mantle structure and are therefore independent

of any dynamic interpretation or assumption of mantle composition, flow, or rheology (viscosity). The average sinking rates imply that slabs move through zones in the mantle with different convective behavior, from an upper mantle that permits, or drives, plate velocities, to a lower mantle in which rates are up to an order of magnitude slower: 10–15 mm/a.

In this paper, we exploit the inferred depth variation in average slab sinking rates to assess the typical magnitude of vertical and horizontal slab velocity and assess the mixing behavior of Earth's mantle. We perform a set of numerical experiments of simplified plate tectonics in a 2D cylindrical geometry in which we vary lower mantle rheology to obtain lithosphere subduction and slab sinking with rates that vary from <10 to >50 mm/a. From these experiments we evaluate the first-order correlation between slab sinking rates and bulk mantle flow. We focus on the long-term (1000 Ma) evolution of bulk mantle flow in terms of typical mantle velocity and the degree of mantle mixing through the potential preservation of mantle heterogeneities.

2. Background

A key mantle property in convection models is the dynamic viscosity, which relates the mechanical stress to the solid-state mantle flow. Various types of observations have been used to obtain a depth-dependant profile of mantle viscosity ([Argus et al., 2021](#); [Čížková et al., 2012](#); [King, 2016](#); [Mitrova and Forte, 2004](#); [Rolf et al., 2018](#);

^{*} Corresponding author.

E-mail address: e.vanderwiel@uu.nl (E. van der Wiel).

Steinberger and Calderwood, 2006) resulting in estimated radial viscosity profiles which can differ by more than an order of magnitude (Fig. 1). Within the currently accepted ranges of mantle properties, numerical models predict semi-layered convection (Kellogg and Turcotte, 1990; Waszek et al., 2021), whole mantle convection (Becker and Faccenna, 2011; Flament et al., 2022), or a hybrid-variant with limited interaction between the upper and lower mantle (Gülcher et al., 2020; Waszek et al., 2021). In such models ambient mantle flow at the base of the mantle can have different magnitudes, indicated by near-stagnant (Bull et al., 2010) or highly mobile (Flament et al., 2022) Large Low Shear Velocity Provinces (LLSVs). This variety in flow magnitudes allow for a well-mixed (Coltice and Schmalz, 2006) or strongly heterogeneous mantle (Barry et al., 2017; Gülcher et al., 2021; van Keken et al., 2002). These variations in mantle convection pattern show that new constraints are desirable to further limit the range of possibilities towards developing more predictive models.

In the last decade, average slab sinking rates have been inferred from the association of geological evidence of the timing of past subduction with large positive seismic velocity anomalies imaged in the modern mantle by seismic tomography (Van Der Meer et al., 2010; Van der Meer et al., 2018). Pioneering studies showed that the geological records of subduction can be used to date the timing of subduction of imaged slab remnants (Faccenna et al., 2003; Hafkenscheid et al., 2006; Replumaz et al., 2004; Van der Voo et al., 1999; van Hinsbergen et al., 2005). Since then, positive seismic wave speed anomalies in tomography have been systematically interpreted and linked to detailed geological reconstructions, whereby shallower (deeper) anomalies are well explained by younger (older) subduction zones. From these correlations, a globally consistent average slab sinking rate of 12 and 13 +/- 3 mm/a has been calculated (Butterworth et al., 2014; Van Der Meer et al., 2010). More recently, the comprehensive, global compilation (Van der Meer et al., 2018) revealed how subducted lithosphere decelerates from plate motion speeds down to an average of 10–15 mm/a in the lower mantle. This

deceleration starts in the mantle transition zone and continues to ~1000–1500 km depth and is consistent with evidence for buckling and thickening of slabs in the same interval (Fuston and Wu, 2021; Sigloch and Mihalyuk, 2013; van Hinsbergen et al., 2005). These correlations suggest that after detachment slabs sink nearly vertically, which is also independently substantiated by static analysis of positive seismic anomalies and locations of paleo-subduction (Domeier et al., 2016). The inferred sinking rates are all confined to a much narrower sinking rate range than the <10 to >50 mm/a that we study in our experiments.

3. Methods

We performed numerical experiments in a 2D cylindrical geometry, simulating global mantle convection during 1000 Ma of subduction evolution. These models are used to obtain slabs varying in size and shape and track their lower mantle sinking rates to compare with the slab sinking rates from (Van der Meer et al., 2018). Our models are purposely simple to solely illustrate the effect of different slab sinking rates, obtained through different lower mantle viscosity profiles, on mantle convection patterns.

3.1. Physical model

In our experiments, we solve the compressible flow equations of mass (Eq. 1), momentum (Eq. 2), and energy conservation (Eq. 3) in a 2D spherical shell. Computations were done using the finite element geodynamic code ASPECT version 2.3.0 (Bangerth et al., 2021; Gassmüller et al., 2018; Heister et al., 2017; Kronbichler et al., 2012), in which we solve for the velocity (u), pressure (P) and temperature (T).

$$\frac{\partial \rho}{\partial t} + \nabla \cdot (\rho u) = 0 \quad (1)$$

$$\nabla \cdot \sigma + \rho g = 0 \quad (2)$$

$$\rho C_p \left(\frac{\partial T}{\partial t} + u \cdot \nabla T \right) - \nabla \cdot (k \nabla T) = \rho H + S_s + S_a + S_l \quad (3)$$

The second and third terms of the energy conservation Eq. (3) account for the advective and diffusive heat transport whereas the right-hand side contains additional heating processes, i.e. radioactive heat production (ρH), shear heating (S_s), adiabatic heating (S_a) and latent heating (S_l) which are coupled to strain rate, thermal expansivity and phase changes in the model, respectively (Schubert et al., 2001; van Zelst et al., 2021).

We use the Isentropic Compression Approximation (ICA), the default approximation for compressible flow in ASPECT (Gassmüller et al., 2020). The ICA neglects the time derivative of the density in the mass conservation equation but does compute a local adiabat based on temperature, pressure, and composition, which results in the alteration of the mass conservation to Eq. (4), where κ_s is the compressibility and ρ the density as function of pressure, temperature, and composition (Gassmüller et al., 2020). Composition dependant material properties are advected through Eq. (5) using compositional fields (c_i).

$$\nabla \cdot u = -\kappa_s \rho g \cdot u \quad (4)$$

$$\frac{\partial c_i}{\partial t} + u \cdot \nabla c_i = 0 \quad (5)$$

3.2. Viscous flow formulation

Flow in our model is governed by the viscous-plastic flow equations that describe dislocation and diffusion creep and we use the Drucker-Prager yield criterion to limit viscous stresses (Glerum et al., 2018). Eq. (6) calculates the diffusion and dislocation creep viscosity which are a function of the effective deviatoric strain rate ($\dot{\epsilon}$), pressure (P), and temperature (T), as well as material properties defined in

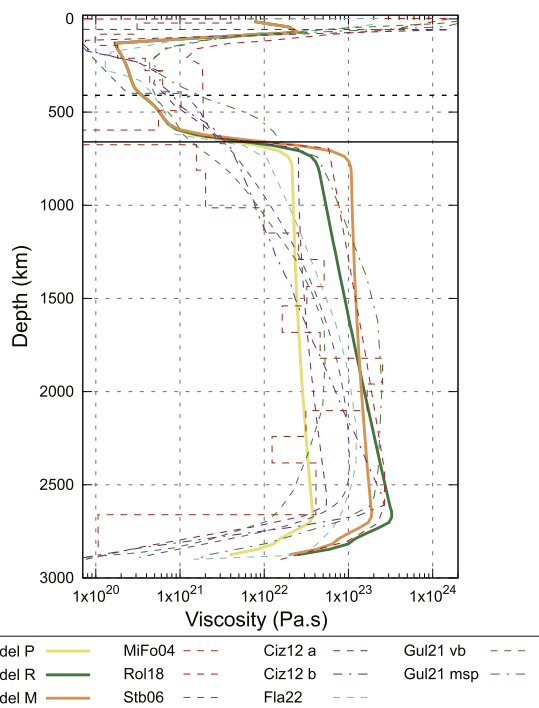


Fig. 1. Radial viscosity profiles for the three models discussed here (solid lines) compared to viscosity profiles as used in other studies: MiFo04 (Mitrovica and Forte, 2004), Stb06 (Steinberger and Calderwood, 2006), Ciz12-a & -b family (Čížková et al., 2012), rol18 case M8 (Rolf et al., 2018), Gul21 viscous blobs (vb) & metastable piles (msp) (Gülcher et al., 2021), Fla22 (Flament et al., 2022).

Supplementary Table 1 (Glerum et al., 2018; Karato and Wu, 1993). The grain-size in the diffusion creep is assumed constant and therefore incorporated in the pre-factor A. Diffusion creep is obtained by setting $n = 1$ in Eq. (6) and dislocation creep by $n = 3$. In the lower mantle flow is based on diffusion creep only.

$$\eta^{cr} = \frac{1}{2} A^{-\frac{1}{n}} \dot{\epsilon}^{-\frac{1-n}{n}} \exp\left(\frac{E + PV}{nRT}\right) \quad (6)$$

$$\sigma_y = C \cos(\phi) + P \sin(\phi) \quad (7)$$

$$\eta^{pl} = \frac{\sigma_y}{2\dot{\epsilon}} \quad (8)$$

$$\eta_{ave}^{cr} = \left(\frac{1}{\eta_{diff}^{cr}} + \frac{1}{\eta_{dist}^{cr}} \right)^{-1} \quad (9)$$

$$\eta^{eff} = \min(\eta^{pl}, \eta_{ave}^{cr}) \quad (10)$$

In 2D the Drucker-Prager yield criterion is similar to the Mohr-Coulomb criterion as shown in Eq. (7) (Glerum et al., 2018). The criterion is parameterised by the cohesion C and angle of internal friction ϕ , where the latter has the same depth dependency as in (Ulvrova et al., 2019). The effective viscosity is rescaled in Eq. (8) to ensure that local stresses cannot exceed the yield stress (Glerum et al., 2018). As both the dislocation and diffusion creep could be active simultaneously, the two are harmonically averaged in Eq. (9) before the effective viscosity (η^{eff}) is calculated in Eq. (10), which is the lowest of either the plastic (η^{pl}) or averaged creep viscosity (η_{ave}^{cr}).

The flow law parameters in the upper mantle (Supplementary Table 1) are constant in all experiments where the pressure and temperature dependence of diffusion creep is based on Ulvrova et al. (2019). This enabled us to obtain self-consistent subduction evolution comprising initiation and cessation of subduction zones. However, in the mantle transition zone (MTZ) we use higher depth-dependency (activation volume) for dislocation creep. We obtain a viscosity in the upper mantle between 10^{20} and 10^{21} Pa s (Fig. 1). To evaluate the effect of different slab sinking rates we vary the lower mantle viscosity in two ways, creating two families of models. We either change the pre-factor (A) or the activation volume (V) in Eq. (6), respectively between $1 - 10 \times 10^{19} \text{ Pa}^{-n} \text{ s}^{-1}$ and $8.34 - 14.34 \times 10^{-7} \text{ m}^3 \text{ mol}^{-1}$ (Supplementary Table 1). These values lead to lower mantle viscosities in our models between 2×10^{22} and 1×10^{24} Pa s (Fig. 1 & Supplementary Fig. 1).

3.3. Setup

Both the inner and outer boundaries are free-slip boundaries, so there is no external kinematic forcing on the model. The resulting existing rotational null space is removed by imposing no-net-rotation of the mantle. The boundaries have fixed temperatures of 3700 K and 300 K. Within the domain two compositional fields are defined: mantle and continent. The mantle domain consists of three different regions separated by the two major phase changes occurring at ~ 410 - and ~ 660 km depths. We use the geodynamic World Builder (Fraters et al., 2019) to set the initial temperature and compositional field distribution. Similar to Ulvrova et al., 2019, we use viscous rafts as ‘continents’ to aid with modelling one-sided subduction systems. We use three continents of 5000, 5000 and 3000 km length, covering roughly 30% of the model surface. To avoid subduction of the continents, we assign the viscous rafts a reference density of 2916 kg/m^3 , which corresponds to a 400 kg/m^3 density contrast with the reference mantle density (Lamb et al., 2020). Furthermore, to avoid deformation of the continents, we assign them a viscosity that equals the maximum cut-off viscosity in the model, i.e. 6×10^{24} Pa s. We also configure three subduction zones and two detached slabs in the initial set-up to seed the model with initial negative buoyancy.

Material properties like thermal expansivity, thermal conductivity

and compressibility are a constant (Supplementary Table 1). We acknowledge this may not be the case for Earth, but exploring the effects of the depth, temperature and compositional dependencies of these parameters is beyond the scope of this study. Through the Rayleigh number we know that a decreasing thermal expansivity and increasing thermal conductivity with depth would lower the vigour of mantle convection, especially in the lowermost mantle (Tosi et al., 2013; Guerrero et al., 2023). However, this vigour should still comply with the inferred average slab sinking rates and therefore in our study this would lead to mantle viscosity profiles somewhat reduced in magnitude to establish the same goal of evaluating the accompanying convective behavior.

The minimal resolution of the mesh in the top 370 km of the modelled domain is ~ 26 km wide cells at the surface, while in the top 1370 km the minimal resolution is a cell width of about ~ 40 km at 1370 km depth. Besides these criteria the mesh refinement is also adaptive, based on viscosity gradients and the velocity field, allowing for refinements up to 13 km wide at the surface. These higher resolutions in the top of the domain allow for accurate modelling of plate-like motion and the initiation of subduction.

3.4. Postprocessing

As we do not prescribe any kinematical boundary conditions in our experiments, we can use the surface velocity of plates to evaluate plate-like motion behavior, assessed by computing the mobility ratio M (Fig. 2c), which is the ratio of surface motion to motion in the entire domain (Eq. 11). When higher than 1, M is deemed indicative of plate-like behavior (Tackley, 2000).

$$M = \frac{V_{rms,surface}}{V_{rms,domain}} \quad (11)$$

We change the rate of slab sinking in the lower mantle by tuning the global lower mantle viscosity (Fig. 1) which we vary by increasing/decreasing the activation volume V , leading to a pressure dependant viscosity increase/decrease with depth, and/or by changing the pre-factor of the diffusion creep law A , leading to an overall shift in the viscosity profiles to lower/higher values, see Eq. (6) and Supplementary Table 1. Modelling 1000 Ma of ocean-ocean and ocean-continent convergence within the cold thermal boundary layer leads multiple subduction zones through time that result in slabs of varying size and shape sinking to the core-mantle boundary (CMB) in each experiment (Fig. 2).

We track the slabs during their mantle journey with passive tracers. Slabs are automatically identified by tracers that move faster than 1 mm/a and have a local temperature that is 300 K lower than the average temperature at depth (Figs. 2b, d and 3a). This temperature threshold is based on estimates of the tomographic visibility of slabs using conversions between seismic velocity anomalies and temperature (Goes et al., 2004; Trampert et al., 2001). 2D-histograms of slab velocity versus depth are constructed from the slab tracers in 5 Ma intervals (Supplementary Movies 1–3). This is done separately for the lateral (Fig. 3b) and radial (Fig. 2e) velocity components using a velocity interval of 2 mm/a and a depth interval of 25. The resulting 200 histograms per experiment are summed to create the accumulated distribution of lateral and radial slab velocities during the 1000 Ma of simulated mantle convection (Fig. 4). Our experiments show that these accumulated histograms gradually become time-stationary. This allows to compute the time-average of *in situ* slab sinking velocity $V(d)$ at mantle depth d from which the average slab sinking rate $V_{ave}(d)$ is obtained with Eq. (12).

$$V_{ave}(d) = \frac{1}{d} \int_0^d V(z) dz \quad (12)$$

$V_{ave}(d)$ represents the model prediction of the average sinking rate for

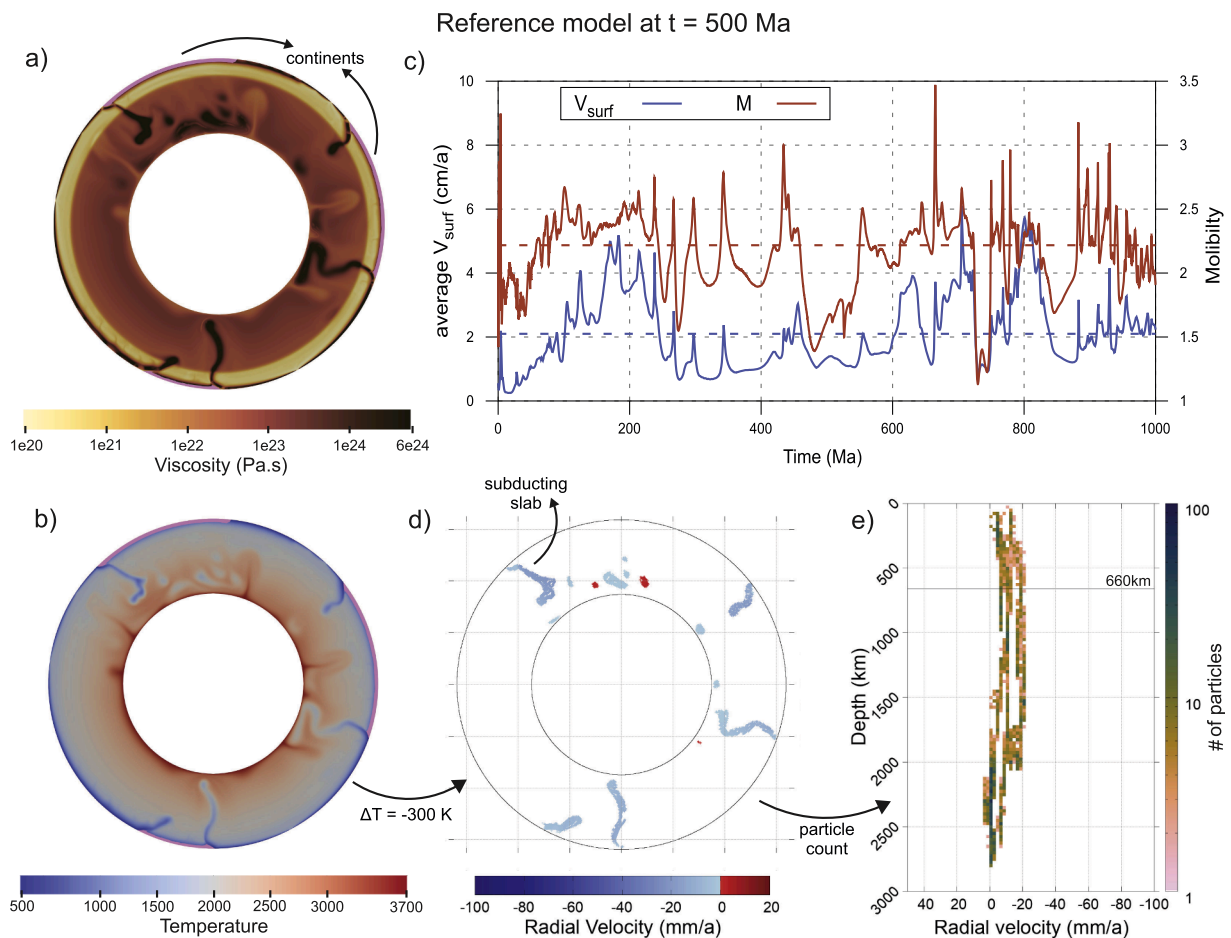


Fig. 2. Results of the reference model (R) after 500 Ma of mantle convection simulation. Snapshots of the model at $t = 500$ Ma are shown for the viscosity (a) and temperature (b) within the modelled domain, showing five slabs actively subducting below the continents (pink). c Solid lines indicate average surface velocity (blue) and mobility ratio M (Tackley, 2000) (red) of model R as well as their dashed time-averages $V_{surf} = 2.1$ cm/a and $M = 2.218$. d Radial velocity of all tracers defined as slabs plotted at their position in the model where blue indicates sinking slabs and red slowly rising. Shown tracers are 300 K colder than the radial averaged temperature at similar depth and automatically obtained (see methods). e 2D-histogram showing the tracer depth vs the radial velocity in 25 km by 2 mm/a bins. The colour indicates the number of particles within a certain bin.

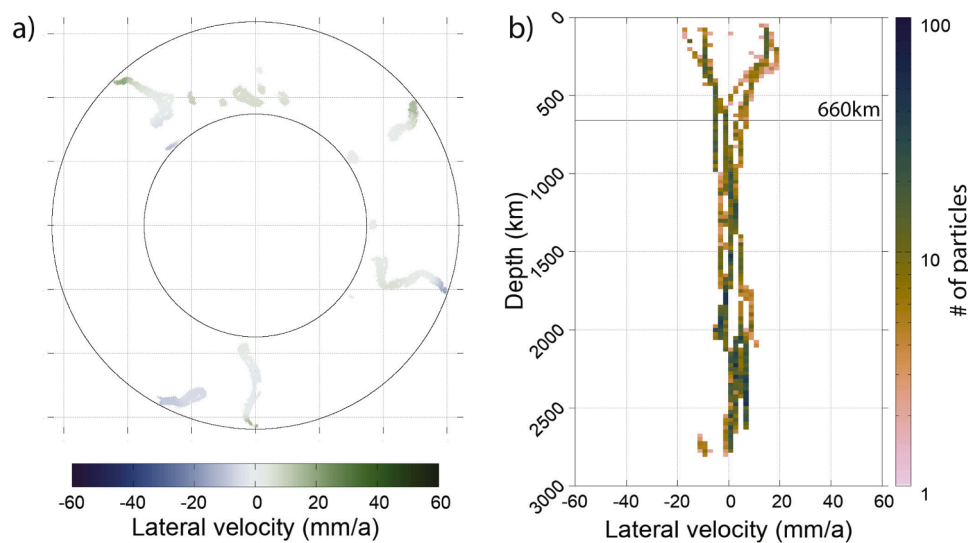


Fig. 3. Lateral slab velocity distribution for the reference model (R) at $t = 500$ Ma. a Lateral velocity of all tracers defined as slabs plotted at their position in the model, where positive (green) values indicate clockwise motion, and negative (blue) values indicate anti-clockwise motion. b 2D-histogram showing particle depth vs lateral slab motion in 25 km by 2 mm/a bins. Colours indicate the number of particles within a certain bin.

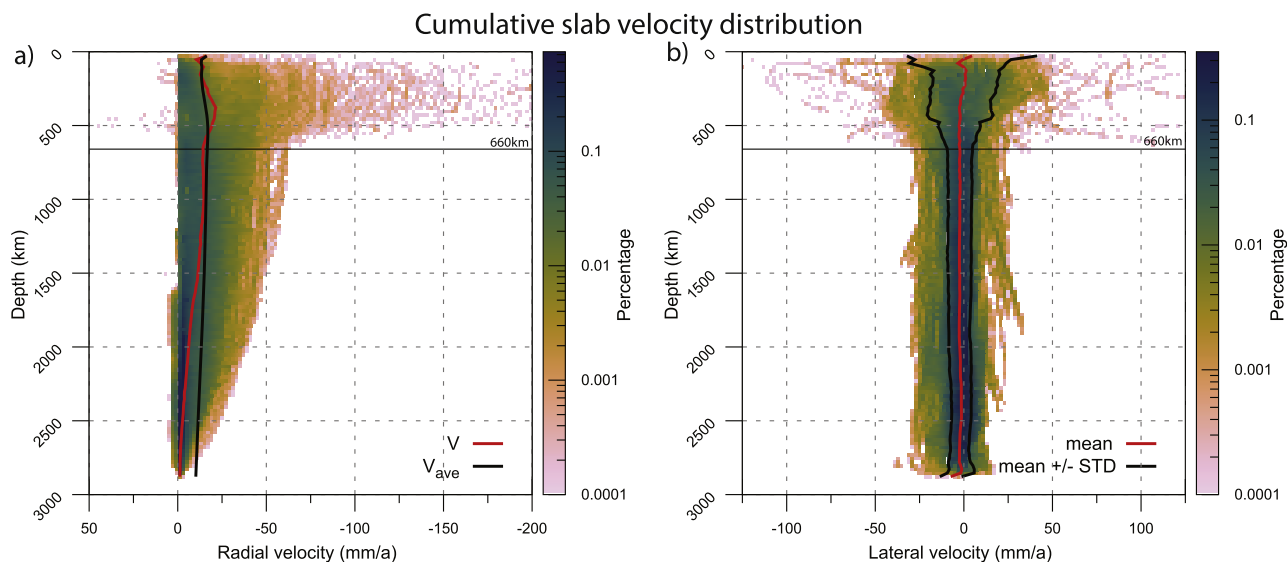


Fig. 4. Slab sinking rate distribution. Summation of all slab velocity distributions from the reference model (R) taken every 5 Ma (see Figs. 1e and 2b and supplementary movie SM 1). The colour scale represents the percentage of all slabs (tracers) that sunk in 1000 Ma of mantle evolution. Tracers defined as slabs can be counted in multiple time intervals. **a** Radial slab velocity distribution with averaged *in situ* radial slab velocities at each depth (red) and integrated slab sinking rate through Eq. (12) (black). **b** Lateral slab velocity distribution in which positive (negative) values indicate (anti-)clockwise motion, mean lateral slab velocity at each depth (red) and mean plus/minus a standard deviation (black) (For interpretation of the references to color in this figure legend, the reader is referred to the web version of this article.).

slabs between the surface and the depth d and can directly be compared to the kinematically inferred average slab sinking rates (Van der Meer et al., 2018).

4. Results

4.1. Natural subduction and plate-tectonic behavior

The surface plate velocities in our experiments are self-generated and are within typical reconstructed ranges of less than 20 cm/a (Zahirovic et al., 2015), and generally below the 10 cm/a. The differences in average plate motion between experiments are small and addressed in the sections below. In all our experiments we obtain lateral plate motions that lead to converging and separation of the cold thermal boundary layer, indicating subduction zones and mid-oceanic ridges. Subduction under the ‘continents’ is one-sided (Fig. 2a, b) and occasionally, in regions with a thin (weak) oceanic lithosphere, intra-oceanic subduction can be two-sided. This occurs through polarity flips of the subduction interface. As our study focusses particularly on the sinking rates of slabs in the lower mantle, the occasional double-sided subduction of the cooled thermal boundary layer material is of no influence on our results. Lateral slab motions in the lower mantle are smaller than their vertical component, indicating that most slabs sink vertically after detachment.

The initially imposed continental regions (Fig. 2a, b) can move away and towards each other, driven by active downwelling of cold material at subduction zones and accommodated by the formation of oceanic ridges. Occasionally this leads to continental collision and break-up of previously collided continents.

Our experiments show the straightforward trend that with increasing lower mantle viscosity the average slab sinking rates $V_{ave}(d)$ decrease. Therefore, we can limit the result description to three models obtained in distinct experiments. First, the reference model R ($A_{df} = 1 \times 10^{-18} Pa^{-1} s^{-1}$, $V_{df} = 12.34 \times 10^{-7} m^3 mol^{-1}$) in which the predicted average slab sinking rates compare well with those kinematically reconstructed (Van der Meer et al., 2018). Second, model M ($A_{df} = 2 \times 10^{-19} Pa^{-1} s^{-1}$, $V_{df} = 8.34 \times 10^{-7} m^3 mol^{-1}$) that provides a marginal sinking rate fit and third, model

P ($A_{df} = 1 \times 10^{-18} Pa^{-1} s^{-1}$, $V_{df} = 8.34 \times 10^{-7} m^3 mol^{-1}$) that exemplifies models yielding a poor match to the sinking rate constraints, with much higher sinking rates than permitted by the data. We will use these three experiments to evaluate the effects of tuning mantle convection models to slab sinking kinematics.

4.2. Reference model R

The average plate velocity along the surface of the reference model R is between 1 and 6 cm/a with a time-averaged mobility ratio M_r of 2.218 (Fig. 2c), which is in the realm of plate-like behavior (Tackley, 2000). The averaged surface velocity is within the typical plate motion ranges reconstructed for the last 200 Ma (Van Der Meer et al., 2014; Zahirovic et al., 2015). The three continents that are initialised in the setup resist subduction and move around laterally along the surface while colliding, diverging, and shielding parts of the subcontinental mantle from active subduction (Supplementary Movie 4).

Slab sinking rates in the uppermost mantle are similar to subducting plate motions, generally below 10 cm/a but occasionally reaching 20 cm/a, again similar to typically reconstructed values (Van Der Meer et al., 2014; Zahirovic et al., 2015). Deceleration of the model slabs starts in the MTZ and continues throughout the lower mantle (Fig. 4a). The averaged *in situ* sinking velocities $V(d)$ has a clear maximum in the upper mantle on top of the MTZ. The first part of the lower mantle shows *in situ* sinking velocities around 15 mm/a up to 1000 km depth before gradually slowing down to 0 mm/a at the CMB (Figs. 4a and 5a). The slab sinking rate $V_{ave}(d)$ decreases from 15 mm/a at the top of the lower mantle to 10 mm/a at the CMB which fits the kinematically reconstructed average sinking rates of 10–15 mm/a (Van der Meer et al., 2018).

Lateral motion of slabs in the upper mantle is mostly restricted between -20 and 20 mm/a (negative (positive) numbers indicate clockwise (anticlockwise) motion in the model) clearly decreasing from the surface to the 660-discontinuity (Fig. 4b). The average lateral velocity in the lower mantle is -2 mm/a with a standard deviation of 5–8 mm/a, dependant on depth, which comprises most (~85%) of the slab-defining tracers (Fig. 4b). This shows that most slabs sink nearly vertically in the reference model.

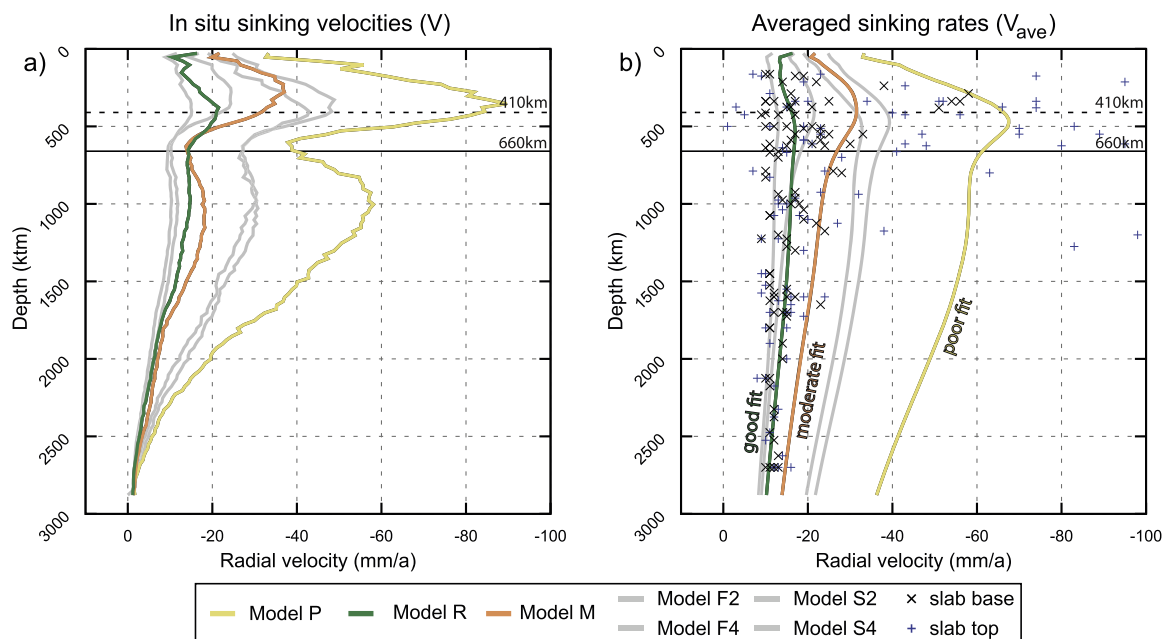


Fig. 5. Profiles of in situ sinking velocities and averaged sinking rates from Eq. (11) matched with the data from Van der Meer et al. (2018). **a** *In situ* sinking velocities calculated as depth average from the cumulative radial slab velocities (Fig. 3a– red line). **b** Averaged slab sinking rates (Fig. 3a– black line) integrated through Eq. (12) (methods) compared to the slab data (Van der Meer et al., 2018) base (plus) and slab top (cross) data. The models with a good fit (model R – green), moderate fit (model M – orange) and poor fit (model P – yellow) are shown in colour together with all other S and F models in grey. The cumulative slab velocity distributions for all models are shown in supplementary Fig. 2 and supplementary Fig. 3 (For interpretation of the references to color in this figure legend, the reader is referred to the web version of this article.).

4.3. Tuning slab sinking rates

Our experiments show that lower mantle viscosity has a small influence on surface plate motions but a first-order impact on slab sinking rates, as exemplified by the models with a poor (P) and moderate (M) fit to the slab sinking rates. Model P is based on a viscosity profile that is generally of smaller amplitude in the lower mantle than the profile of model R (Fig. 1), while the profile of model M has higher viscosities in the top part of the lower mantle and lower values in the bottom part (Fig. 1). Models P and M have similar averaged mobility factors ($M_p=2.215$, $M_m=2.332$, resp.) as model R ($M_r=2.218$). The spherically averaged surface velocities in model P and M are larger than in model R, generally between 1 and 10 cm/a. A contrast between the model predictions occurs mainly in the attained slab sinking rates. Model P results in a poor match to the inferred slab sinking rates exemplified by the four times larger maximum *in situ* sinking velocity (Fig. 6), because of the lower mantle viscosity in model P (Fig. 1). Excess peak-velocities in model P occur in the upper mantle and around 1000 km depth, where *in situ* sinking velocities reach highest values up to 60 mm/a (Fig. 5a and Supplementary Fig. 2). The large difference *in situ* velocities between models P and R translates into a large difference in average sinking rates. Model P has average sinking rates between 40 and 60 mm/a (Fig. 5b and Supplementary Fig. 3), about four times higher than in model R.

Subduction in model M leads to average sinking rates in the lower mantle that are comparable to the faster side of inferred sinking rate values (Fig. 5b). Model M has an average lower mantle viscosity that is only slightly increasing with depth, from $\sim 10^{23}$ Pa·s in the top of the lower mantle to $\sim 2 \cdot 10^{23}$ Pa·s in the deep lower mantle (Supplementary Fig. 1). The maximum *in situ* sinking velocity in model M is twice as large as in the reference model R, up to 35 mm/a in the upper mantle (Fig. 5a and Supplementary Fig. 2). The sinking velocities in the lower mantle are, again, highest around 1000 km depth where slabs in model M sink with a depth-averaged *in situ* velocity of ~ 18 mm/a. The average slab sinking rates of model M are above 20 mm/a in the upper part of the lower mantle while decreasing to 14 mm/a near the CMB (Fig. 5b).

The lateral motion of slabs in the lower mantle is directly correlated to the sinking rates, models with slabs that sink fastest also show a greater variability in lateral motion across the mantle. Broadly distributed lateral velocities over 100 mm/a occur in the entire lower mantle of model P (Supplementary Fig. 2) and although the lateral average remains close to the centre at ~ 2 –3 mm/a, the standard deviation is with 18–22 mm/a, varying with depth, in the lower mantle three times larger than in the reference model R. Model M occasionally has lateral slab velocities over 20 mm/a in the lower mantle, however, the histograms shows a narrow distribution with standard deviations of maximum 10 mm/a (Supplementary Fig. 2).

4.4. Mantle flow and mixing

In our models, cold slabs are the main drivers of mantle flow, and their sinking triggers hot upwellings from the lower thermal boundary layer. Over geological time this leads to mantle mixing, the efficiency of which depends on the vigour of mantle convection. We analyze the overall evolution of mantle motion, as well as mixing, by tracking predefined tracer clouds over time in three different ways. First, we track how 4 circular tracer clouds at 0 Ma are dispersed through time in steps of 250 Ma (Fig. 6a, b). Second, we investigate the positions at 0 Ma, and at every 250 Ma, of tracers that aggregate in the same 4 circular regions after 1000 Ma of model evolution (Fig. 6c, d). Third, to visualize mixing in the entire mantle, we track all initial 100,000 tracers, colour coded as function of their radius at 0 Ma. Fig. 7a–d show all tracers at 500 Ma and 1000 Ma and Supplementary Movies 4–6 show the mantle flow and mixing through time in steps of 5 Ma. Furthermore, we track the number of tracers that have been entrained in the upper mantle or in the lithosphere (configured as the top 100 km of the modelling domain) or stayed in the lower mantle in 1000 Ma of model evolution (Fig. 8).

The dispersion of tracers in models R and M is similar: both models have large provinces of tracers that move in unison for the first 500 Ma of convection. These coherently moving mantle volumes deform while moving slowly through the lower mantle but can be dispersed and

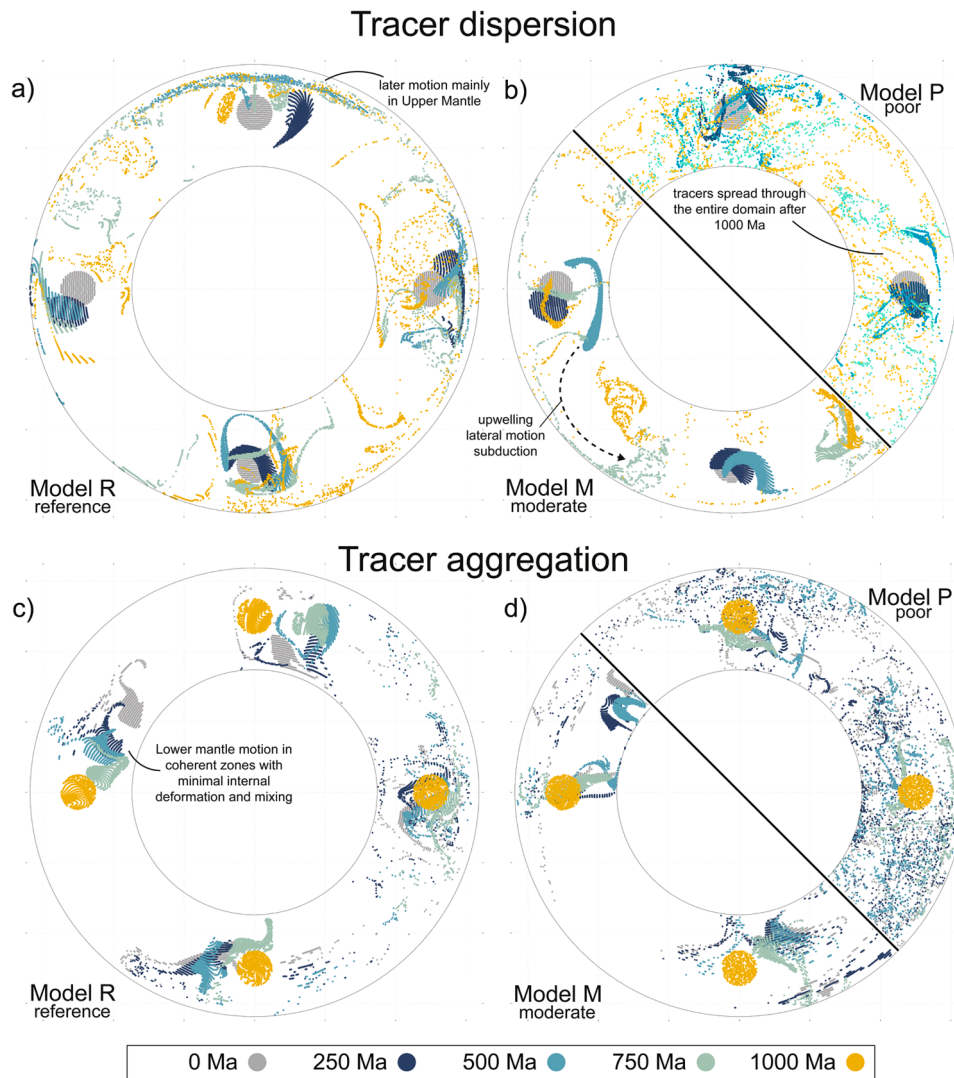


Fig. 6. Motion of the mantle shown through individual tracers in 250 Ma steps. Tracers that move from (disperse) or move to (aggregate) four pre-defined circles. **a-b** Tracer dispersion and **c-d** aggregation for the Reference model (model R) with good fit to the data and models M and P with a moderate and poor fit.

stretched when a slab sinks through (Fig. 6a, b). Most lateral motion and dispersion of these tracers occurs after their entrainment in the upper mantle or lithosphere (Fig. 6b). Accordingly, tracers that never enter the upper mantle undergo little dispersion in the mantle. In model R, some tracers only moved by ~ 2000 km in 1000 Ma of convection (Fig. 6a), which gives an average non-slab mantle velocity of 2 mm/a. Both model R and M have mantle provinces that remain in the mid-mantle and that show no or little mixing throughout the modelled 1000 Ma time period. An increased tracer cloud stretching and dispersing is observed in Model P, signalling stronger mixing. After 1000 Ma, tracers are mixed throughout the mantle and are more randomly distributed over the entire mantle domain as compared to models R and M (Fig. 6a, b).

The same holds for the aggregating tracers of model P. At 0 Ma the tracers that will end up in the four yellow circular regions after 1000 Ma of mantle evolution are distributed throughout the entire mantle. After 750 Ma of convection only part of those tracers have aggregated into irregular shaped zones (Fig. 6d). This means that in the last 250 Ma significant mantle motion must still occur to form final tracer configuration of yellow circular regions.

This is entirely different in the more viscous model M, which shows a convective vigour where many tracers at 0 Ma already form irregular shaped closely packed clouds of tracers. Over time those tracer clouds will further deform into their final circular shape at 1000 Ma. This shows

that their original mantle composition is being preserved (Fig. 6d), i.e., with limited or no mixing. In the last 500 Ma of convection in model M, most tracers reside in the lower mantle and are within ~ 3000 km of their final destination, giving a maximum non-slab lower mantle flow rate of 6 mm/a. Model R's convective pattern is even slower, most of the aggregating tracers have moved coherently since 0 Ma and seem to never enter the upper mantle and their average distance travelled is lower than 4000 km in 1000 Ma of convection giving an averaged flow speed of less than 4 mm/a (Fig. 6c).

After 500 Ma, model R has large accumulations of subducted initial lithosphere near the CMB while the removed lithosphere at the surface has been formed out of material that mostly originated from the initial upper mantle (Fig. 7a). Adjacent to the piles of subducted initial lithosphere at the CMB, lower mantle material has started upwelling, but most parts of the lower mantle still have retained their initial internal structure. Model M shows similar features of lower mantle evolution, although the upper mantle is more mixed, especially below the collided continental keels (Fig. 7b). In contrast, after 500 Ma in Model P, the subducted lithosphere material is much less accumulated near the CMB and has been mixed upward by return flows leading to preservation in slivers throughout the lower mantle, albeit near their subduction location. And although the lower mantle is not well-mixed after 500 Ma, it does not show the propensity of preserving large coherent areas of

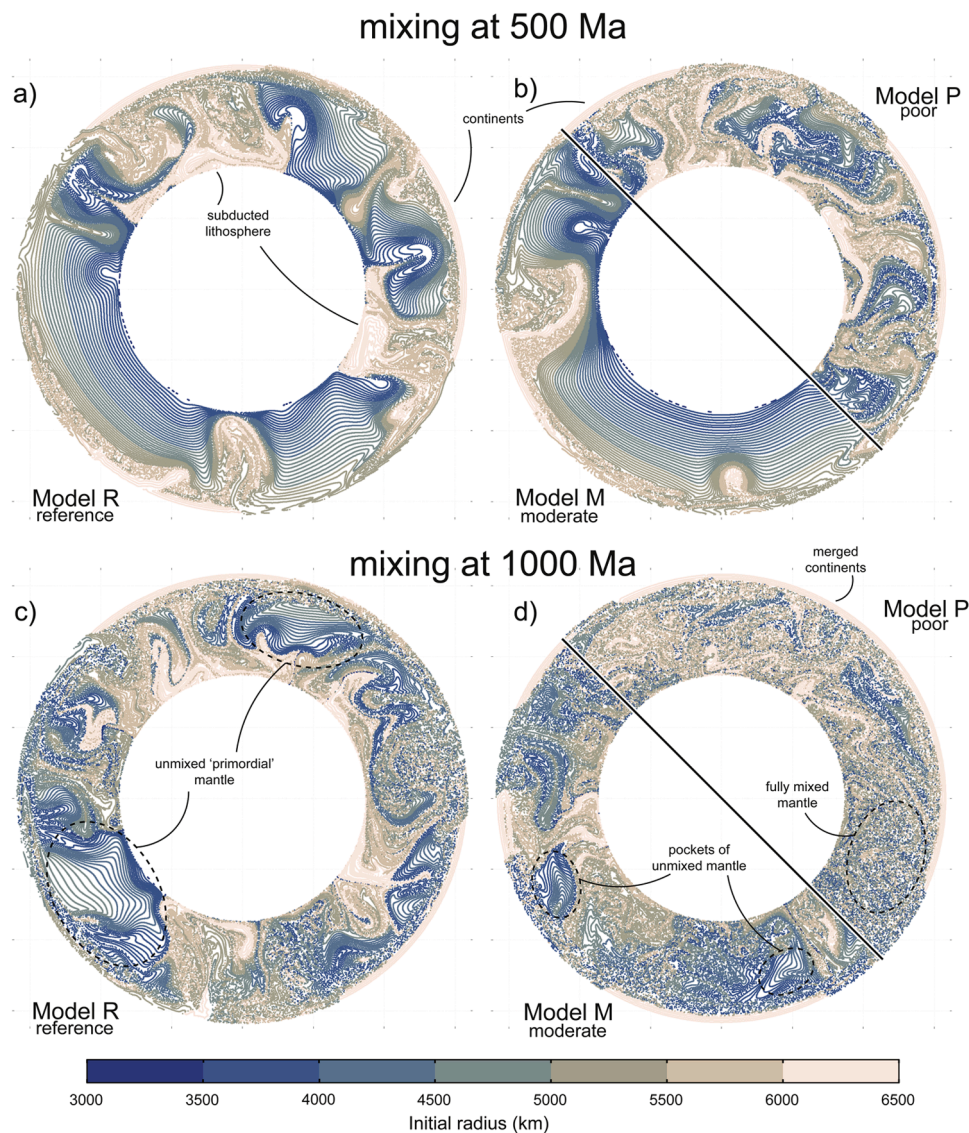


Fig. 7. Mixing of the mantle for the three models at 500 (a–b) and 1000 (c–d) Ma of simulated convection. Shown are all tracers within each model coloured by their radius at $t = 0$ Ma.

‘primordial’ mantle structure as seen in the other two models. The lower mantle experiences more deformation and more zones of upwelling bring material from the lowermost mantle to the surface (Figs. 7b, 8a). 18% of all tracers have been entrained in the lithosphere at least once and 40% of the lower mantle material has remained there after 500 Ma (Fig. 8a, b). In models M and R, these ratios are equal with 13% of tracers that have been part of the lithosphere while more than 45% of tracers remained in the lower mantle (Fig. 8c–f).

After 1000 Ma of subduction and convection the differences between model P, and the models R and M have increased. Model P shows no tendency for preservation of large regions of primordial mantle (less than 10%, Fig. 8b) as the mantle is largely mixed and initial lithosphere material has been stirred through the entire mantle with only a few stretched slivers remaining (Fig. 7d, 8a and Supplementary Movie 6). For model P, more than 40% of tracers have been part of the lithosphere during the model evolution, indicating a high degree of mixing (Fig. 8b). Model R contains preserved zones of mixed mantle as well as zones of unmixed, ‘primordial’ mantle. The initially subducted lithosphere has been pushed around near the CMB and in the lower mantle while occasionally also brought back to the surface through plume-like upwellings (Supplementary Movie 4). The unmixed zones preserve their

original internal structure, have varying sizes and occur at all depth in the lower mantle (Fig. 7c, 8e). Here, about 25% of the tracers have been preserved in the lower mantle while only 20% has been entrained in the lithosphere (Fig. 8f). Finally, model M has a similar preservation as model R although the preserved unmixed mantle is less abundant (only 13%, Fig. 8d), and the zones are smaller (Figs. 7d, 8c). Pockets of unmixed mantle can enter the upper mantle but are then fast entrained in lateral ‘surface’ flow, like plate motions, before being mixed back into the mantle during subduction (Supplementary Movie SM 5).

5. Discussion

Our experiments illustrate that average slab sinking rates are strongly linked to the long-term vigour of mantle convection. Models with lower slab sinking rates showcase a low propensity for mixing by mantle flow such that large and slowly deforming regions in the mantle remain unmixed after 1000 Ma of mantle evolution (Fig. 7c, 8e). Using average slab sinking rates as an additional constraint that needs to be matched by geodynamic models provides a promising opportunity to advance to more ‘Earth-like’ mantle models with better determined mantle viscosity, and mantle flow and mixing properties.

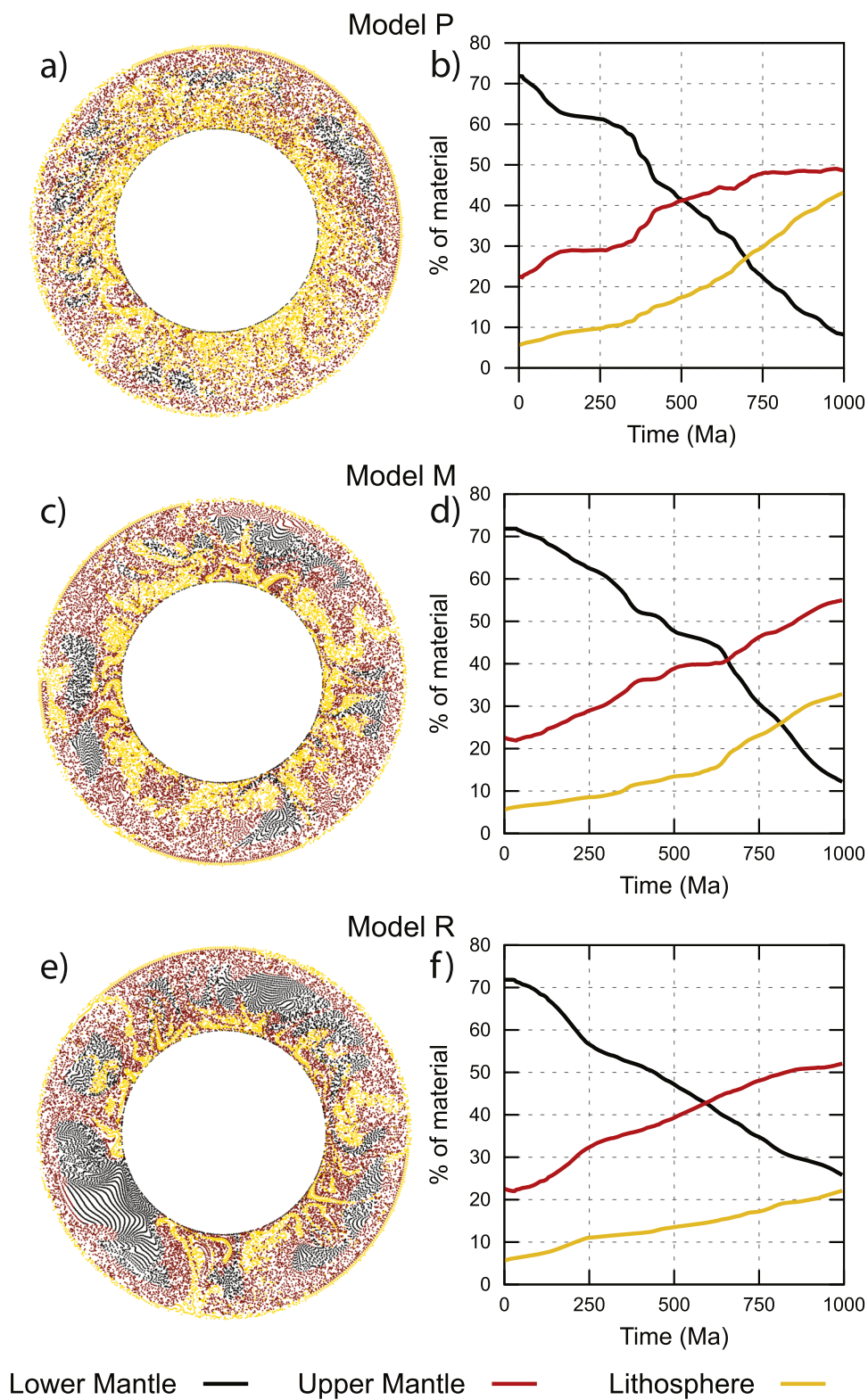


Fig. 8. Mixing of the mantle of the three models at 1000 Ma (left) and the relative abundance of three compositions (right). The compositional distribution is based on radius of the tracers, with the Lower Mantle (black) below 660 km, Upper Mantle (red) below 100 km and lithosphere (yellow) in the top 100 km. Lower mantle tracers can get entrained in the upper mantle and subsequently in the lithosphere but not visa-versa. Therefore, the percentage of lower mantle material can only decrease and the percentage of lithosphere material can only increase (For interpretation of the references to color in this figure legend, the reader is referred to the web version of this article.).

We deliberately use simplified models and parameters because we primarily aim to demonstrate the benefit of using the inferred average slab sinking velocity for narrowing the range in the vigour of mantle convection. The lower mantle viscosity of our preferred model (model R) is on the high-end of the estimated ranges (King, 2016; Mitrovica and Forte, 2004; Steinberger and Calderwood, 2006) but similar to other recent geodynamic studies (Fig. 1) (Čížková et al., 2012; Flament et al., 2022; Gülcher et al., 2021; Rolf et al., 2018). However, most of these studies use a decreasing thermal expansivity and increasing thermal conductivity with depth, which both lead to a smaller density contrast between slab and mantle and thus a gradual reduction of slab buoyancy with depth (Tosi et al., 2013). Qualitatively, to match the inferred sinking rates, a gradual reduction in slab buoyancy would generally imply a gradual depth-dependant reduction of the mantle viscosities. This may explain our higher lower mantle viscosity, roughly by a factor 2, than the first study matching slab sinking rates (Čížková et al., 2012), although we also assess a broader spatial and temporal spectrum of subducted slabs than a single slab system as in Čížková et al., 2012. We do not expect that when the slab buoyancy is reduced, due to the decreasing thermal expansivity and increasing thermal conductivity, the convective vigour of our models will change, as we would tune our preferred viscosity profile to comply to the same average sinking rates.

Other rheological simplifications in our models are that chemical or compositional heterogeneities that are present in the Earth's mantle are not represented in our experiments. Our slabs have the same rheological properties as the bulk mantle, and once the negative buoyancy that makes our slabs sink disappears by thermal conduction, they assimilate to the warm mantle and do not inherit any density or chemical signal as recycled oceanic crust in the model. In reality, also thermally assimilated slabs are likely still compositionally distinct from the bulk mantle (Jones et al., 2021; Lambart et al., 2019). The same holds true for primordial mantle material, which is compositionally distinct from bulk mantle (Jackson et al., 2021). This may be one of the reasons why thermochemical structures, such as LLSVPs or ULVZs that are probably not purely thermal features (Garnero et al., 2016; Koelemeijer et al., 2017; McNamara, 2019), do not develop in our models. Nonetheless, it is interesting to evaluate how mixing and motion behavior in our reference model R, that is successfully tuned to slab sinking kinematics, compares with models that address current debates on Earth's interior dynamics, like LLSVP stability, mantle heterogeneity, or plume dynamics (Arnould et al., 2020; Cao et al., 2021; Flament et al., 2022; Gülcher et al., 2021; Jones et al., 2021; Mulyukova et al., 2015).

The fate of subducted oceanic lithosphere might be strongly connected to structures in the lower mantle, as they may form thermochemical piles on the CMB (Jones et al., 2021) that may overlap with or correspond to LLSVPs or ULVZs (Ballmer et al., 2016; Dobson and Brodholt, 2005). Our models R and M seem to preserve former slabs in thick piles on the CMB (Fig. 7a, b). These modelled piles are strongly tied to the convective vigour of the mantle rather than being a characteristic feature of our slabs. For instance, in model P, with high sinking rates of 40–60 mm/a, such piles do not form (Fig. 7b). We observe that in parts of the model without actively sinking slabs, mantle flow is minimal, allowing preservation of more or less stagnant piles of subducted lithosphere, even though in our models subducted material is not compositionally distinct. We foresee that adding compositional heterogeneity to our models may further enhance this behavior.

Because of the, purely thermal, density differences in slabs, the piles on the CMB do move and get entrained in mantle flow, whereby mantle flow is controlled by slab sinking and close to the CMB by horizontal slab motion (Fig. 7c, d). In models R and M, horizontal slab motion in the lower mantle is limited and slabs sink nearly vertically (Fig. 4b and Supplementary Figs. 2 and 3), and thus only interact with the ambient mantle in their direct surroundings. The average velocity of the lowermost mantle (bulk mantle and slabs) in model R is lower than 4 mm/a, well below the sinking rate of slabs. The slowly convecting mantle in our models provides a straightforward explanation for the stability of

lowermost mantle structures including the LLSVPs (Burke and Torsvik, 2004; Torsvik et al., 2010, 2014) and slab graveyard compositions (Jackson and Macdonald, 2022) that follow from kinematic correlations.

Conversely, our model P, with higher sinking rates, also has faster horizontal slab motions, with standard deviations around 20 mm/a, three times higher than in model R. In that respect, the rates of sinking and mantle flow in model P resemble those in model experiments that were used to argue for strong horizontal motions of slabs in the mantle, which in turn would be able to shovel lower mantle structures such as LLSVPs along the CMB (Cao et al., 2021; Flament et al., 2022; Lin et al., 2022; Peng and Liu, 2022). The comparison between our models P and R suggests that tuning models to reconstructed slab sinking behavior may strongly influence the conclusions on lower mantle mobility and horizontal slab motion during sinking.

Finally, it is interesting to note that even after a billion years of subduction and convection the mantle in our experiments tuned to slab sinking rates preserve large blobs of unmixed, 'primordial' mantle. These are in the heart of major, slow, mantle convective systems in the lower to mid-mantle (Fig. 7c). These primordial provinces in our experiments resemble structures that were proposed before as compositionally distinct zones that could be more rigid (Ballmer et al., 2017; Gülcher et al., 2020). In our experiments, provinces of subducted lithosphere forming piles and primordial provinces forming mid-mantle blobs simply result from the slow bulk mantle convection rate that results from tuning the model against slab sinking. This illustrates that much lower mantle convection rates than typically generated in numerical models may explain many of the outstanding puzzles on long-lived structural and compositional heterogeneity. Adding further complexity to mantle convection models, such as compositional, thermal and depth variations of thermal conductivity and expansivity (Guerrero et al., 2023; Tosi et al., 2013) and compositionally dependant viscosity in the lower mantle (Ballmer et al., 2017; Gülcher et al., 2021; Yamazaki and Karato, 2001) may further enhance the patterns we observe in our experiments, as the rheological contrast between different compositions may influence the mixing behavior (Manga, 1996). Our models are based on the commonly used linear diffusion rheology of the lower mantle. This does not include shear localization as a local agent for mantle mixing. Propositions for nonlinear lower mantle rheologies are few (e.g., Cordier et al. 2023; Girard et al. 2016) and how these would impact mantle flow and mantle mixing is yet to be established. Arguably, if shear localization would occur around sinking slabs then this would decouple slab sinking from the ambient mantle to a higher degree than in our models with linear rheology and thus could lead to a lower mixing of the ambient mantle than modelled here.

Nonetheless, our results, with a compositionally homogeneous mantle, show that tuning geodynamic models to match the average slab sinking rates for the last 250 Ma provides a novel avenue towards explaining the survival of large, primordial mantle reservoirs. Furthermore, models with too high slab sinking rates might systematically overestimate bulk mantle flow and the vigour of convection. This suggests that adding new kinematic correlations between geochemistry, seismology, and geology as constraint on mantle convection models is an important step in improving our dynamic models and their predictive value.

6. Conclusions

In this study, using 2D cylindrical mantle modelling, we have explored how the recent inferred average slab sinking rates can help narrow determining the long-term average magnitude of mantle flow velocity and the propensity for mantle mixing. Models with low mantle slab sinking rates of 10–15 mm/a have very limited bulk mantle motion, of only a few mm/a, and after 1000 Ma of subduction evolution and mantle convection these models preserve large zones of unmixed regions in the mid-mantle. Therefore, the addition of new inferred kinematic observations or constraints to mantle convection models can provide

avenues to explain the magnitude and pattern of mantle convection and the large-scale preservation of geochemical mantle reservoirs.

CRedit authorship contribution statement

Erik van der Wiel: Writing – original draft, Visualization, Methodology, Investigation, Conceptualization. **Douwe J.J. van Hinsbergen:** Conceptualization, Supervision, Writing – review & editing. **Cedric Thieulot:** Methodology, Writing – review & editing. **Wim Spakman:** Writing – review & editing, Methodology.

Declaration of Competing Interest

The authors declare that they have no known competing financial interests or personal relationships that could have appeared to influence the work reported in this paper.

Data availability

Data will be made available on request.

Acknowledgments

This work was supported by the Netherlands Organisation for Scientific Research (NWO Vici Grant 865.17.001). We thank the Computational Infrastructure for Geodynamics (<http://geodynamics.org>) which is funded by the National Science Foundation under awards EAR-0949446, EAR-1550901, and EAR-2149126. We thank F. Capitanio and an anonymous reviewer for their constructive feedback and helpful suggestions.

Supplementary materials

Supplementary material associated with this article can be found, in the online version, at [doi:10.1016/j.epsl.2023.118471](https://doi.org/10.1016/j.epsl.2023.118471).

References

- Argus, D.F., Peltier, W.R., Blewitt, G., Kreemer, C., 2021. The viscosity of the top third of the lower mantle estimated using GPS, GRACE, and relative sea level measurements of glacial isostatic adjustment. *J. Geophys. Res. Solid Earth* 126 (5), e2020JB021537. <https://doi.org/10.1029/2020JB021537>.
- Arnould, M., Coltice, N., Flament, N., Mallard, C., 2020. Plate tectonics and mantle controls on plume dynamics. *Earth Planet. Sci. Lett.* 547, 116439 <https://doi.org/10.1016/j.epsl.2020.116439>.
- Ballmer, M.D., Houser, C., Hernlund, J.W., Wentzcovitch, R.M., Hirose, K., 2017. Persistence of strong silica-enriched domains in the Earth's lower mantle. *Nat Geosci* 10 (3), 236–240. <https://doi.org/10.1038/NGEO2898>.
- Ballmer, M.D., Schumacher, L., Lekic, V., Thomas, C., Ito, G., 2016. Compositional layering within the large low shear-wave velocity provinces in the lower mantle. *Geochem. Geophys. Geosyst.* 17 (12), 5056–5077. <https://doi.org/10.1126/sciadv.1500815>.
- Bangerth, W., Dannberg, J., Fraters, M., Gassmüller, R., Glerum, A., Heister, T., & Naliboff, J. (2021). ASPECT v2.3.0. Zenodo. [10.1029/2018GC007508](https://doi.org/10.1029/2018GC007508).
- Barry, T., Davies, J., Wolstencroft, M., Millar, I., Zhao, Z., Jian, P., Safonova, I., Price, M., 2017. Whole-mantle convection with tectonic plates preserves long-term global patterns of upper mantle geochemistry. *Sci. Rep.* 7 (1), 1–9. <https://doi.org/10.1038/s41598-017-01816-y>.
- Becker, T.W., Faccenna, C., 2011. Mantle conveyor beneath the Tethyan collisional belt. *Earth Planet. Sci. Lett.* 310 (3–4), 453–461. <https://doi.org/10.1016/j.epsl.2011.08.021>.
- Bercovicci, D., Schubert, G., Ricard, Y., 2015. Abrupt tectonics and rapid slab detachment with grain damage. *Proc. Natl. Acad. Sci.* 112 (5), 1287–1291.
- Bull, A., McNamara, A., Becker, T., Ritsema, J., 2010. Global scale models of the mantle flow field predicted by synthetic tomography models. *Phys. Earth Planet. Interiors* 182 (3–4), 129–138. <https://doi.org/10.1016/j.pepi.2010.03.004>.
- Burke, K., Torsvik, T.H., 2004. Derivation of large igneous provinces of the past 200 million years from long-term heterogeneities in the deep mantle. *Earth Planet. Sci. Lett.* 227 (3–4), 531–538. <https://doi.org/10.1016/j.epsl.2004.09.015>.
- Butterworth, N., Talsma, A., Müller, R., Seton, M., Bunge, H.P., Schubert, B., Shephard, G., Heine, C., 2014. Geological, tomographic, kinematic and geodynamic constraints on the dynamics of sinking slabs. *J. Geodyn.* 73, 1–13. <https://doi.org/10.1016/j.jog.2013.10.006>.
- Cao, X., Flament, N., Müller, R.D., 2021. Coupled evolution of plate tectonics and basal mantle structure. *Geochem. Geophys. Geosyst.* 22 (1), e2020GC009244 <https://doi.org/10.1029/2020GC009244>.
- Čížková, H., van den Berg, A.P., Spakman, W., Matyska, C., 2012. The viscosity of Earth's lower mantle inferred from sinking speed of subducted lithosphere. In: *Phys. Earth Planet. Interiors*, 200, pp. 56–62. <https://doi.org/10.1016/j.pepi.2012.02.010>.
- Coltice, N., Schmalz, J., 2006. Mixing times in the mantle of the early Earth derived from 2-D and 3-D numerical simulations of convection. *Geophys. Res. Lett.* 33 (23) <https://doi.org/10.1029/2006GL027707>.
- Coltice, N., Seton, M., Rolf, T., Müller, R., Tackley, P.J., 2013. Convergence of tectonic reconstructions and mantle convection models for significant fluctuations in seafloor spreading. *Earth Planet. Sci. Lett.* 383, 92–100. <https://doi.org/10.1016/j.epsl.2013.09.032>.
- Cordier, P., Gouriet, K., Weidner, T., Van Orman, J., Castelnaud, O., Jackson, J.M., Carrez, P., 2023. Periclase deforms more slowly than bridgmanite under mantle conditions. *Nature* 613 (7943), 303–307.
- Dobson, D.P., Brodholt, J.P., 2005. Subducted banded iron formations as a source of ultralow-velocity zones at the core–mantle boundary. *Nature* 434 (7031), 371–374. <https://doi.org/10.1038/nature03430>.
- Domeier, M., Doubrovine, P.V., Torsvik, T.H., Spakman, W., Bull, A.L., 2016. Global correlation of lower mantle structure and past subduction. *Geophys. Res. Lett.* 43 (10), 4945–4953. <https://doi.org/10.1002/2016GL068827>.
- Faccenna, C., Jolivet, L., Piromallo, C., Morelli, A., 2003. Subduction and the depth of convection in the Mediterranean mantle. *J. Geophys. Res. Solid Earth* 108 (B2). <https://doi.org/10.1029/2001JB001690>.
- Flament, N., Bodur, Ö.F., Williams, S.E., Merdith, A.S., 2022. Assembly of the basal mantle structure beneath Africa. *Nature* 603 (7903), 846–851. <https://doi.org/10.1038/s41586-022-04538-y>.
- Fraters, M., Thieulot, C., Van Den Berg, A., Spakman, W., 2019. The geodynamic world builder: a solution for complex initial conditions in numerical modeling. *Solid Earth* 10 (5), 1785–1807. <https://doi.org/10.5194/se-10-1785-2019>.
- Fuston, S., Wu, J., 2021. Raising the Resurrection plate from an unfolded-slab plate tectonic reconstruction of northwestern North America since early Cenozoic time. *GSA Bull.* 133 (5–6), 1128–1140. <https://doi.org/10.1130/B35677.1>.
- Garnero, E.J., McNamara, A.K., Shim, S.H., 2016. Continent-sized anomalous zones with low seismic velocity at the base of Earth's mantle. *Nat. Geosci.* 9 (7), 481–489. <https://doi.org/10.1038/NGEO2733>.
- Gassmüller, R., Dannberg, J., Bangerth, W., Heister, T., Myhill, R., 2020. On formulations of compressible mantle convection. *Geophys. J. Int.* 221 (2), 1264–1280. <https://doi.org/10.1093/gji/ggaa078>.
- Gassmüller, R., Lokavarapu, H., Heien, E., Puckett, E.G., Bangerth, W., 2018. Flexible and scalable particle-in-cell methods with adaptive mesh refinement for geodynamic computations. *Geochem. Geophys. Geosyst.* 19 (9), 3596–3604. <https://doi.org/10.1029/2018GC007508>.
- Girard, J., Amulele, G., Farla, R., Mohiuddin, A., Karato, S.I., 2016. Shear deformation of bridgmanite and magnesiowüstite aggregates at lower mantle conditions. *Science* 351 (6269), 144–147.
- Glerum, A., Thieulot, C., Fraters, M., Blom, C., Spakman, W., 2018. Nonlinear viscoplasticity in ASPECT: benchmarking and applications to subduction. *Solid Earth* 9 (2), 267–294. <https://doi.org/10.5194/se-9-267-2018>.
- Goes, S., Cammarano, F., Hansen, U., 2004. Synthetic seismic signature of thermal mantle plumes. *Earth Planet. Sci. Lett.* 218 (3–4), 403–419. [https://doi.org/10.1016/S0012-821X\(03\)00680-0](https://doi.org/10.1016/S0012-821X(03)00680-0).
- Gülcher, A.J., Gebhardt, D.J., Ballmer, M.D., Tackley, P.J., 2020. Variable dynamic styles of primordial heterogeneity preservation in the Earth's lower mantle. *Earth Planet. Sci. Lett.* 536, 116160 <https://doi.org/10.1016/j.epsl.2020.116160>.
- Guerrero, J.M., Deschamps, F., Li, Y., Hsieh, W.-P., Tackley, P.J., 2023. Influence of heterogeneous thermal conductivity on the long-term evolution of the lower-mantle thermochemical structure: implications for primordial reservoirs. *Solid Earth* 14 (2), 119–135. <https://doi.org/10.5194/se-14-119-2023>.
- Gülcher, A.J.P., Ballmer, M.D., Tackley, P.J., 2021. Coupled dynamics and evolution of primordial and recycled heterogeneity in Earth's lower mantle. *Solid Earth* 12 (9), 2087–2107. <https://doi.org/10.5194/se-12-2087-2021>.
- Hafkenscheid, E., Wortel, M., Spakman, W., 2006. Subduction history of the Tethyan region derived from seismic tomography and tectonic reconstructions. *J. Geophys. Res. Solid Earth* 111 (B8). <https://doi.org/10.1029/2005JB003791>.
- Heister, T., Dannberg, J., Gassmüller, R., Bangerth, W., 2017. High accuracy mantle convection simulation through modern numerical methods—II: realistic models and problems. *Geophys. J. Int.* 210 (2), 833–851. <https://doi.org/10.1093/gji/ggx195>.
- Jackson, M., Becker, T., Steinberger, B., 2021. Spatial characteristics of recycled and primordial reservoirs in the deep mantle. *Geochem. Geophys. Geosyst.* 22 (3), e2020GC009525 <https://doi.org/10.1029/2020GC009525>.
- Jackson, M., Macdonald, F., 2022. Hemispheric geochemical dichotomy of the mantle is a legacy of austral supercontinent assembly and onset of deep continental crust subduction. *AGU Adv.* 3 (6), e2022AV000664 <https://doi.org/10.1029/2022AV000664>.
- Jones, T.D., Sime, N., van Keken, P., 2021. Burying Earth's primitive mantle in the slab graveyard. *Geochem. Geophys. Geosyst.* 22 (3), e2020GC009396 <https://doi.org/10.1029/2020GC009396>.
- Karato, S.I., Wu, P., 1993. Rheology of the upper mantle: a synthesis. *Science* 260 (5109), 771–778. <https://doi.org/10.1126/science.260.5109.771>.
- Kellogg, L., Turcotte, D., 1990. Mixing and the distribution of heterogeneities in a chaotically convecting mantle. *J. Geophys. Res. Solid Earth* 95 (B1), 421–432. <https://doi.org/10.1029/JB095iB01p00421>.

- King, S.D., 2016. Reconciling laboratory and observational models of mantle rheology in geodynamic modelling. *J. Geodyn.* 100, 33–50. <https://doi.org/10.1016/j.jog.2016.03.005>.
- Koelmeijer, P., Deuss, A., Ritsema, J., 2017. Density structure of Earth's lowermost mantle from Stoneley mode splitting observations. *Nat. Commun.* 8 (1), 1–10. <https://doi.org/10.1038/ncomms15241>.
- Kronbichler, M., Heister, T., Bangerth, W., 2012. High accuracy mantle convection simulation through modern numerical methods. *Geophys. J. Int.* 191 (1), 12–29. <https://doi.org/10.1111/j.1365-246X.2012.05609.x>.
- Lamb, S., Moore, J.D., Perez-Gussinye, M., Stern, T., 2020. Global whole lithosphere isostasy: implications for surface elevations, structure, strength, and densities of the continental lithosphere. *Geochem. Geophys. Geosyst.* 21 (10), e2020GC009150 <https://doi.org/10.1029/2020GC009150>.
- Lambart, S., Koornneef, J.M., Millet, M.A., Davies, G.R., Cook, M., Lissenberg, C.J., 2019. Highly heterogeneous depleted mantle recorded in the lower oceanic crust. *Nat. Geosci.* 12 (6), 482–486. <https://doi.org/10.1038/s41561-019-0368-9>.
- Lin, Y.A., Colli, L., Wu, J., 2022. NW Pacific-Panthalassa intra-oceanic subduction during Mesozoic times from mantle convection and geoid models. *Geochem. Geophys. Geosyst.*, e2022GC010514 <https://doi.org/10.1029/2022GC010514>.
- Manga, M., 1996. Mixing of heterogeneities in the mantle: effect of viscosity differences. *Geophys. Res. Lett.* 23 (4), 403–406. <https://doi.org/10.1029/96GL00242>.
- McNamara, A.K., 2019. A review of large low shear velocity provinces and ultra low velocity zones. *Tectonophysics* 760, 199–220. <https://doi.org/10.1016/j.tecto.2018.04.015>.
- Mitrovica, J., Forte, A., 2004. A new inference of mantle viscosity based upon joint inversion of convection and glacial isostatic adjustment data. *Earth Planet. Sci. Lett.* 225 (1–2), 177–189. <https://doi.org/10.1016/j.epsl.2004.06.005>.
- Mulyukova, E., Steinberger, B., Dabrowski, M., Sobolev, S.V., 2015. Survival of LLSVPs for billions of years in a vigorously convecting mantle: replenishment and destruction of chemical anomaly. *J. Geophys. Res. Solid Earth* 120 (5), 3824–3847. <https://doi.org/10.1002/2014JB011688>.
- Peng, D., Liu, L., 2022. Quantifying slab sinking rates using global geodynamic models with data-assimilation. *Earth Sci. Rev.* 104039 <https://doi.org/10.1016/j.earscirev.2022.104039>.
- Replumaz, A., Karason, H., van der Hilst, R.D., Besse, J., Tapponnier, P., 2004. 4-D evolution of SE Asia's mantle from geological reconstructions and seismic tomography. *Earth Planet. Sci. Lett.* 221 (1–4), 103–115.
- Ritsema, J., Lekić, V., 2020. Heterogeneity of seismic wave velocity in Earth's mantle. *Annu. Rev. Earth Planet Sci.* 48, 377–401. <https://doi.org/10.1146/annurev-earth-082119-065909>.
- Rolf, T., Capitanio, F.A., Tackley, P.J., 2018. Constraints on mantle viscosity structure from continental drift histories in spherical mantle convection models. *Tectonophysics* 746, 339–351. <https://doi.org/10.1016/j.tecto.2017.04.031>.
- Schubert, G., Turcotte, D.L., Olson, P., 2001. *Mantle Convection in the Earth and Planets*. Cambridge University Press. <https://doi.org/10.1017/CBO9780511612879>.
- Sigloch, K., Mihalynuk, M.G., 2013. Intra-oceanic subduction shaped the assembly of Cordilleran North America. *Nature* 496 (7443), 50–56. <https://doi.org/10.1038/nature12019>.
- Steinberger, B., Calderwood, A.R., 2006. Models of large-scale viscous flow in the Earth's mantle with constraints from mineral physics and surface observations. *Geophys. J. Int.* 167 (3), 1461–1481. <https://doi.org/10.1111/j.1365-246X.2006.03131.x>.
- Tackley, P.J., 2000. Self-consistent generation of tectonic plates in time-dependent, three-dimensional mantle convection simulations. *Geochem. Geophys. Geosyst.* 1 (8) <https://doi.org/10.1029/2000GC000036>.
- Torsvik, T.H., Burke, K., Steinberger, B., Webb, S.J., Ashwal, L.D., 2010. Diamonds sampled by plumes from the core–mantle boundary. *Nature* 466 (7304), 352–355. <https://doi.org/10.1038/nature09216>.
- Torsvik, T.H., van der Voo, R., Doubrovine, P.V., Burke, K., Steinberger, B., Ashwal, L.D., Trønnes, R.G., Webb, S.J., Bull, A.L., 2014. Deep mantle structure as a reference frame for movements in and on the Earth. *Proc. Natl. Acad. Sci.* 111 (24), 8735–8740. <https://doi.org/10.1073/pnas.1318135111>.
- Tosi, N., Yuen, D.A., de Koker, N., Wentzcovitch, R.M., 2013. Mantle dynamics with pressure- and temperature-dependent thermal expansivity and conductivity. *Phys. Earth Planet. Interiors* 217, 48–58. <https://doi.org/10.1016/j.pepi.2013.02.004>.
- Trampert, J., Vacher, P., Vlaar, N., 2001. Sensitivities of seismic velocities to temperature, pressure and composition in the lower mantle. *Phys. Earth Planet. Interiors* 124 (3–4), 255–267. [https://doi.org/10.1016/S0031-9201\(01\)00201-1](https://doi.org/10.1016/S0031-9201(01)00201-1).
- Ulvrova, M.M., Coltice, N., Williams, S., Tackley, P.J., 2019. Where does subduction initiate and cease? A global scale perspective. *Earth Planet. Sci. Lett.* 528, 115836 <https://doi.org/10.1016/j.epsl.2019.115836>.
- Van Der Meer, D.G., Spakman, W., Van Hinsbergen, D.J., Amaru, M.L., Torsvik, T.H., 2010. Towards absolute plate motions constrained by lower-mantle slab remnants. *Nat. Geosci.* 3 (1), 36–40. <https://doi.org/10.1038/ngeo708>.
- Van der Meer, D.G., Van Hinsbergen, D.J., Spakman, W., 2018. Atlas of the underworld: slab remnants in the mantle, their sinking history, and a new outlook on lower mantle viscosity. *Tectonophysics* 723, 309–448. <https://doi.org/10.1016/j.tecto.2017.10.004>.
- Van Der Meer, D.G., Zeebe, R.E., van Hinsbergen, D.J., Sluijs, A., Spakman, W., Torsvik, T.H., 2014. Plate tectonic controls on atmospheric CO₂ levels since the Triassic. *Proc. Natl. Acad. Sci.* 111 (12), 4380–4385. <https://doi.org/10.1073/pnas.1315657111>.
- Van der Voo, R., Spakman, W., Bijwaard, H., 1999. Tethyan subducted slabs under India. *Earth Planet. Sci. Lett.* 171 (1), 7–20. [https://doi.org/10.1016/S0012-821X\(99\)00131-4](https://doi.org/10.1016/S0012-821X(99)00131-4).
- van Hinsbergen, D.J.J., Hafkenscheid, E., Spakman, W., Meulenkamp, J., Wortel, R., 2005. Nappe stacking resulting from subduction of oceanic and continental lithosphere below Greece. *Geology* 33 (4), 325–328. <https://doi.org/10.1130/G20878.1>.
- van Keken, P.E., Hauri, E.H., Ballentine, C.J., 2002. Mantle mixing: the generation, preservation, and destruction of chemical heterogeneity. *Annu. Rev. Earth Planet Sci.* 30 (1), 493–525. <https://doi.org/10.1146/annurev.earth.30.091201.141236>.
- van Zelst, I., Cramer, F., Pusok, A.E., Glerum, A., Dannberg, J., Thieulot, C., 2021. 101 Geodynamic modelling: how to design, carry out, and interpret numerical studies. *Solid Earth Discussions*, pp. 1–80. <https://doi.org/10.5194/se-13-583-2022>.
- Waszek, L., Tauzin, B., Scherrer, N.C., Ballmer, M.D., Afonso, J.C., 2021. A poorly mixed mantle transition zone and its thermal state inferred from seismic waves. *Nat. Geosci.* 14 (12), 949–955. <https://doi.org/10.1038/s41561-021-00850-w>.
- Yamazaki, D., Karato, S.I., 2001. Some mineral physics constraints on the rheology and geothermal structure of Earth's lower mantle. *Am. Mineral.* 86 (4), 385–391. <https://doi.org/10.2138/am-2001-0401>.
- Yan, J., Ballmer, M.D., Tackley, P.J., 2020. The evolution and distribution of recycled oceanic crust in the Earth's mantle: insight from geodynamic models. *Earth Planet. Sci. Lett.* 537, 116171 <https://doi.org/10.1016/j.epsl.2020.116171>.
- Zahirovic, S., Müller, R.D., Seton, M., Flament, N., 2015. Tectonic speed limits from plate kinematic reconstructions. *Earth Planet. Sci. Lett.* 418, 40–52. <https://doi.org/10.1016/j.epsl.2015.02.037>.